An improved dynamic bidirectional coupled hydrologic-hydrodynamic model for efficient flood inundation prediction

Yanxia Shen, Zhenduo Zhu, Qi Zhou, Chunbo Jiang*

State Key Laboratory of Hydroscience and Engineering, Department of Hydraulic Engineering, Tsinghua University, Beijing, 100084, China

Abstract: To improve computational efficiency while maintaining numerical accuracy, coupled hydrologic-hydrodynamic models based on non-uniform grids are used for flood inundation prediction. In those models, a hydrodynamic model using a fine grid can be applied for flood-prone areas, and a hydrologic model using a coarse grid can be used for the rest of the areas. However, it is challenging to deal with the separation and interface between the two types of areas because the boundaries of the flood-prone areas are time-dependent. We present an improved Multigrid Dynamical Bidirectional Coupled hydrologic-hydrodynamic Model (IM-DBCM) with two major improvements: 1) automated non-uniform mesh generation based on the D∞ algorithm was implemented to identify the flood-prone areas where high-resolution inundation conditions are needed; 2) ghost cells and bilinear interpolation were implemented to improve numerical accuracy in interpolating variables between the coarse and fine grids. A hydrologic model, two-dimensional (2D) nonlinear reservoir model was bidirectionally coupled with a 2D hydrodynamic model that solves the shallow water equations. Three cases were considered to demonstrate the effectiveness of the improvements. In all cases, the mesh generation algorithm was shown to efficiently and successfully generate high-resolution grids in those flood-prone areas. Compared with the original M-DBCM (OM-DBCM), the new model had lower RMSEs and higher

*Corresponding author: State Key Laboratory of Hydroscience and Engineering, Department of Hydraulic Engineering, Tsinghua University, Beijing, 100084, China
Corresponding author: Tel: +8613581891886; E-mail address: jcb@tsinghua.edu.cn

NSEs, indicating that the proposed mesh generation and interpolation were reliable and stable. It can be adapted adequately to the real-life real flood evolution process in watersheds and provide practical and reliable solutions for rapid flood prediction.

Key words: Coupled hydrologic-hydrodynamic model; Multi-grid generation; Bilinear interpolation; Computational efficiency and accuracy; Flood simulation

1 Introduction

Floods are the most frequent natural disasters that seriously harm human health and economic growth. Numerical models are critical for predicting flooding processes to help prevent or mitigate the damaging effects of floods on people and communities (Bates, 2022). Coupled hydrologic-hydrodynamic models are widely used to translate the amount of rainfall obtained from weather forecasting models or rain gauge observations into surface inundation (Xia et al., 2019).

Coupled hydrologic-hydrodynamic models can be generally divided into external (one-way) and internal (two-way) coupling models (see Figure 1). The external coupling models utilize hydrographs obtained from hydrologic models as an input for hydrodynamic models in a fixed position, providing a one-way transition (Schumann et al., 2013; Feistl et al., 2014; Choi and Mantilla, 2015; Bhola, 2018; Wing et al., 2019). It is powerful tools for watershed flood simulation, in particular large spatial and temporal scale, due to its convenience in model construction. However, this one-way flow information cannot capture the mutual interaction between runoff production and flood inundation, and the fixed interface is inconsistent with the actual flood process where the inflow discharge positions, flow path, and discharge values change with accumulating rainfall.

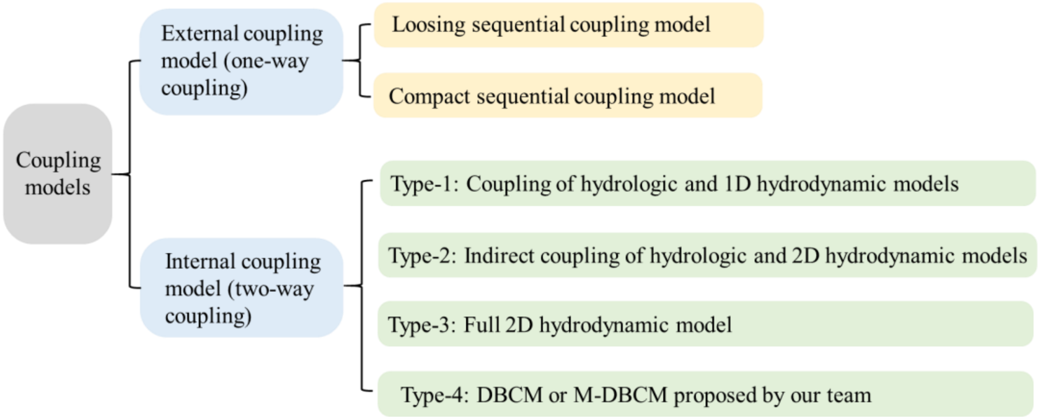

Figure 1 Classifications of coupled hydrologic and hydrodynamic models

The two-way coupling models are further divided into: the coupled hydrologic-1D hydrodynamic model (HH1D), indirect coupled hydrologic-2D hydrodynamic models (ICM2D), full 2D hydrodynamic models (HM2D), and dynamic bidirectional coupling model (DBCM or M-DBCM) proposed by author's team. In the HH1D, the discharges obtained from the hydrologic model is treated as mass source of the 1D hydrodynamic model, while the water depth calculated in 1D hydrodynamic model is fed back to hydrologic model, such as the coupled Mike SHE and Mike 11 (Thompson et al., 2004). The application of 1D modeling of overland flow is limited when developing precise and reliable flood maps in 2D inundation regions.

In order to overcome the lack of 2D hydrodynamic simulation in HH1D, the ICM2D is proposed, where the runoff first flows into 1D rivers, and then discharge into the 2D inundation regions (Seyoum et al., 2012; Chen et al., 2017 and 2018). For example, Mike SHE and Mike11 are coupled to form Mike Urban, and Mike11 and Mike21 are dynamically coupled to form Mike Flood. The indirect coupling between the hydrologic and the 2D hydrodynamic models can be developed by coupling Mike Urban and Mike Flood. The 1D hydrodynamic model is a connection channel between the hydrologic and the 2D hydrodynamic models. Compared with the HH1D, this coupling type has satisfactory and acceptable accuracy and is widely used. As the 2D hydrodynamic model is only calculated in local inundation regions, its computational efficiency is greatly improved in comparison with the HM2D. However, the ICM2D assumed that the water first discharges into the 1D rivers, and then flows from 1D rivers to the 2D regions. The hydrologic model is not directly coupled with the 2D hydrodynamic model, which is inconsistent with the actual flood processes. In reality, water may be discharged into both 1D channel and 2D waterbodies simultaneously, and the hydrologic, 1D and 2D hydrodynamic models should be linked directly. Direct coupling of hydrologic and 2D hydrodynamic models can physically reflect the flood processes, which deserves more attention.

In HM2D, the 2D hydrodynamic model is used to simulate the overland flow (runoff routing and flood inundation), and the runoff generation serves as its mass source term (Singh et al., 2011; Garcia-Navarro et al., 2019; Hou et al., 2020; Costabile and Costanzo, 2021). It has satisfactory and acceptable numerical accuracy and has been widely used. But the development and simulation of HM2D require high-resolution topographic data at the catchment scale and extensive computational time, which hinder their application in large-scale flood forecasting (Kim et al., 2012). In HEC-RAS (US Army Corps of Engineers, 2023), for instance, the flooding process in 1D rivers was simulated by a 1D hydrodynamic model, whereas the flooding process in 2D regions was simulated using 2D diffusion wave equations (DWEs) or shallow water equations (SWEs). If the 2D regions were discretized into finer grids and the 2D SWEs was applied, the 1D hydrodynamic model was coupled with the 2D SWEs. It has high numerical accuracy but is computationally prohibitive for large-scale applications. Conversely, if the 2D regions were discretized into coarse grids and the 2D DWEs was applied, the 1D hydrodynamic model was coupled with the 2D DWEs, which can expand the application scale at the cost of reducing the accuracy.

Jiang et al. (2021) proposed a DBCM based on uniform structured grids, where the hydrologic and 2D hydrodynamic models were coupled in a two-way manner and the coupling interface of these two models was time-dependent. The model can automatically evolve the surface flow and fully consider the flow states with both mass and momentum transfer. However, because uniform grids were adopted in DBCM, it inevitably increased the computational cost and time, especially in the large watershed.

An essential consideration to reduce computational time is mesh coarsening (Caviedes-Voullième et al., 2012). Adaptive mesh refinement (AMR) has been used to optimize the grid resolution during flood simulations (Donat et al., 2014; Hu et al., 2018; Ghazizadeh, 2020; Ding et al., 2021; Kesserwani and Sharifian, 2023). Aiming to increase computational efficiency by reducing computing nodes, it adjusts grid size for local grid refinement by domain features or flow conditions. Yu (2019) used quadtree grids to divide the computational domain and applied the DBCM to simulate the flooding process. It needs to segment and merge the grid elements repeatedly during the calculation, which can be time-consuming and offset the calculation time saved by the optimized grid. Besides, the mesh generation and flood simulation were compiled in the same code base, which increased the computation cost and time.

Static non-uniform grids have increasingly received attention in recent years, which simplified grid generation procedure compared with AMR (Caviedes-Voullième et al., 2012; Hou et al., 2018; Bomers et al., 2019; Ozgen-Xian et al., 2020). Compared with uniform grids and AMR, it can not only reduce computational nodes, but use different time steps in different grid sizes to further reduce computation time. Shen et al. (2021) and Shen and Jiang (2023) divided the computational domain based on static multi-grids, where the different grid size ratios of coarse to fine grids were designed. But there were two limitations to this scheme. One limitation is that the grids need to be generated manually, which can be subjective and uncertain. It also needs a heavy workload, especially for large watersheds. Besides the grid generation, the variable interpolation between the coarse and fine cells was also not reasonable. There are shared and hanging nodes at the interpolation interface. Shen et al. (2021) assumed the variables at the shared nodes were equal to that at the cell center, and the hanging nodes were calculated by the shared nodes. The results showed that this scheme has unsatisfactory accuracy and frequently fails to converge. Although the multi-grid-based model can reduce computational time, there are remarkable challenges such as the grid partition technique, determination of coarse and fine regions, and variables interpolation between coarse and fine grids.

The objective of this study is to develop an integrated system that fully couples the hydrologic and 2D hydrodynamic models, utilize an automated method for efficient multi-grid mesh generation, and resolve variable interpolation between coarse and fine grids more accurately. An improved dynamic bidirectional coupling model (IM-DBCM) was presented, where the 2D nonlinear reservoir (NLR) model was coupled with the 2D hydrodynamic model through a CMI. The D∞ algorithm was implemented to divide the computational domain into non-uniform grids automatically. Ghost cells (i.e., the virtual cells located on the boundaries of the computational domain) and bilinear interpolation were used to interpolate variables between the coarse and fine grids. Three case studies were conducted, and the simulation results were compared with the original M-DBCM (OM-DBCM) to evaluate the effectiveness of the improvements.

2 Methodology

The Fortran programming language was adopted to apply the coupling model. The framework of IM-DBCM is illustrated in Figure 1. The model consists of two components: a hydrologic model (i.e., 2D NLR) that simulates the runoff generation and routing, and 2D hydrodynamic model simulating the flood inundation process. Before the model setup, it is required to first design the grids. For the model execution, the variables interpolation between coarse and fine grids and the coupling of hydrologic and hydrodynamic models are the two main issues that must be addressed.

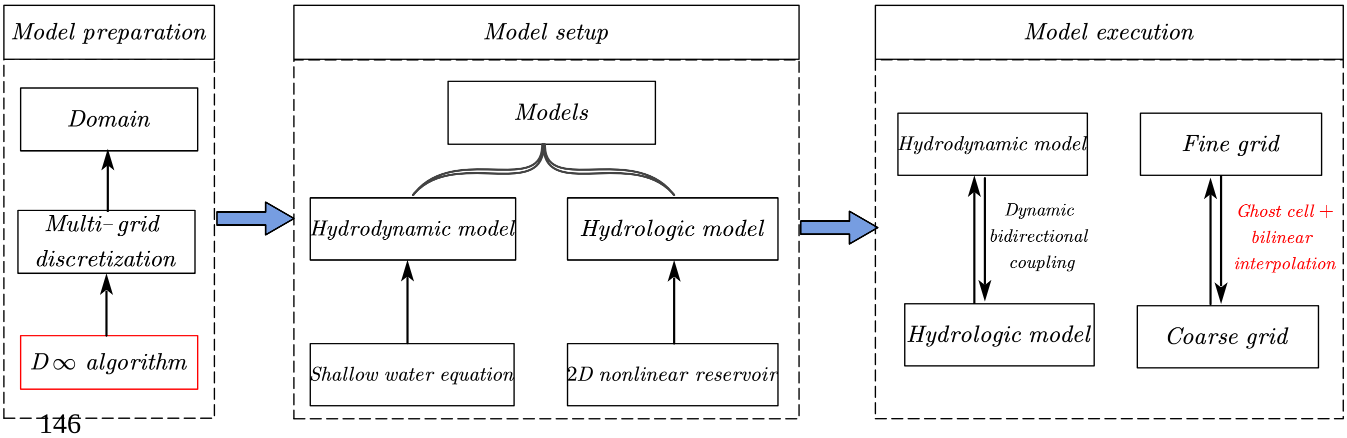

Figure 1 Framework of IM-DBCM

2.1 Automated multi-grid generation

Associated with flood models, the design of computational grids that are scalable and suitable for all applications is challenging. The grid generation can be considered as a model preprocess, which is the foundation of flood simulation and can influence both computational accuracy and efficiency. In this study, a multi-grid generation method was proposed based on the D∞ algorithm, to generate refined grid cells at flood-prone areas where high-resolution representation of topographic features is essential for flood simulation while discretizing the rest of the domain using coarse grids. The D∞ algorithm is a method of representing flow directions based on triangular facets in grid DEM proposed by Tarboton (1997). It allocates the flow fractionally to each lower neighboring grid in proportion to the slope toward that grid. The flow direction is determined as the direction of the steepest downward slope on the eight triangular facets formed across a 3×3-pixel window centered on the pixel of interest, which was detailed by Tarboton (1997). Compared with the D8 algorithm, where the flow is discretized into only one of eight possible directions, separated by 45°, the D∞ algorithm is more reasonable and accurate for delineating the actual river trend.

The process of discretizing computational domain based on the D∞ algorithm is shown in Figure 2. First, a raw DEM was prepared, and sink filling was performed on the DEM. Second, the D∞ algorithm was applied to determine the flow direction on grids. Subsequently, the upslope area, defined as the total catchment area that is upstream of a grid center or short length of contour (Moore et al., 1991), was calculated based on the flow direction. Finally, an area threshold was defined to identify the slope lands and derive the river drainage networks from accumulated drainage areas. In a grid cell, if the upslope area was larger than the predefined threshold, it was considered as a river drainage network; otherwise, it was defined as slope lands. The generated slope lands and river network were verified through field surveys or satellite images-based estimates. Generally, the river drainage networks present low slopes and hydraulic conveyance, which is subject to flooding. Therefore, these areas should be discretized using fine grids to represent the flooding process in high resolution. However, in the slope lands, fine grids were not required and coarse grids were used to improve computational efficiency. Because the regions of interest were of high resolution, the reliability of the prediction would not deteriorate, although the number of grid cells was considerably reduced, which can increase model efficiency and capability for flood simulations over large domains. Compared with manual work, the grid generation based on the D∞ algorithm can both reduce workload and time.

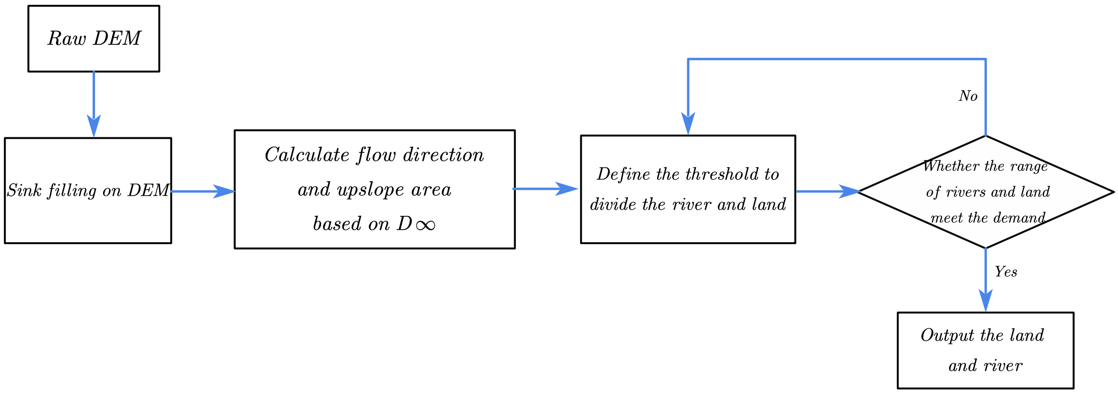

Figure 2 Grid generation based on the D∞ algorithm

A schematic of grid generation is shown in Figure 3. Two types of connecting interfaces are presented, which divide the computing domain into three parts. The first type is the red line (Variable Interpolation Interface, VII) between the coarse and fine grids. The grid cell size changes suddenly on both sides of this line. The second type (Coupling Moving Interface, CMI) is marked in blue on fine grids, which is moving and time-dependent. The first part represents the coarse-grid areas, where the hydrologic model is used to simulate rainfall-runoff. The other two parts are located in the fine-grid areas. The regions between VII and CMI are defined as intermediate transition zones, where the hydrologic model is used to simulate the flooding process. These transition zones facilitate the application of different time steps in different grid cell sizes to improve computational efficiency. The hydrologic and hydrodynamic models are dynamically coupled to represent the flooding process on fine grids, and the CMI is a coupling boundary.

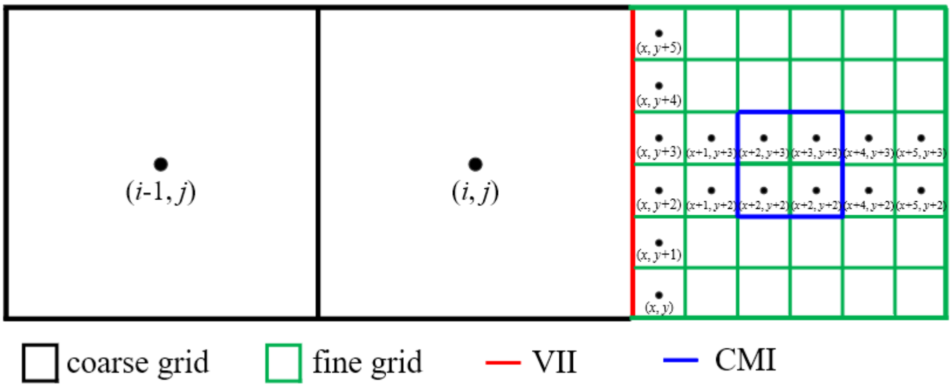

Figure 3. Schematic diagram of grid generation, where *i* and *j* are the coordinates of coarse grid; *x* and *y* are the coordinates of fine grid; VII is the Variable Interpolation Interface and CMI is the Coupling Moving Interface

2.2 Variable interpolation between coarse and fine grids

During a flow computation, if a cell has a neighbor of different size, interpolation may be required to approximate variables in certain locations so that the governing equation can be solved smoothly. An example is presented in Figure 4(a), where the coarse grid has two eastern neighbors that are half its size. In this case, the variable values of the smaller cells are obtained from those of larger cells. In the traditional method, these variables are directly calculated using certain interpolation methods. There are shared (P_1, P_2) and hanging (Q) nodes at the interface between the coarse and fine grids. In Shen et al. (2021), the variable values on shared nodes can be transmitted directly, while the values on hanging nodes were obtained by linear interpolation of the shared nodes. This method is simple, feasible and easy to use. However, the variable values are stored at the cell center, and there are no values at the interface nodes. Shen et al. (2021) assumed that the values at the interface nodes were equal to that at the cell center. It is inaccurate to make such an assumption, which can bring errors. And the resulting error will increase as the cell size increases.

To overcome these drawbacks, ghost cells and bilinear interpolation method were used to interpolate variables between coarse and fine grids.

Figure 4(a) shows the variable interpolation between the coarse and fine grids. Two ghost fine cells were created, which were overlaid with partial coarse grids. The variables on the ghost fine cells were interpolated through the coarse and fine grids between the interface, which were then used as the boundary conditions for the calculation of the fine grids at the next time step. The bilinear interpolation method was applied. The variable interpolation may involve variables at locations c_1 , c_2 , c_3 , f'_{v1}, f'_{v2}, f_1 and f_2 . As the variables are stored at the cell center, the variables at c_1 , c_2 , c_3 , f_1 and f_2 are available directly. The values at f'_{v1} and f'_{v2} are obtained via natural neighbor interpolation, as follows:

$$U_{f'_{v1}} = U_{c_1} + \frac{U_{c_2} - U_{c_1}}{y_{c_2} - y_{c_1}} (y_{f'_{v1}} - y_{c_1}) \quad (1)$$

$$U_{f'_{v2}} = U_{c_3} + \frac{U_{c_1} - U_{c_3}}{y_{c_1} - y_{c3}} (y_{f'_{v2}} - y_{c_3}) \quad (2)$$

where $U_{f'_{v1}}, U_{f'_{v2}}, U_{c_1}, U_{c_2}, U_{c_3}$ are the variables at locations f'_{v1}, f'_{v2}, c_1, c_2, c_3 respectively; $y_{f'_{v1}}, y_{f'_{v2}}, y_{c_1}, y_{c_2}, y_{c_3}$ are the coordinates in y directions at f'_{v1}, f'_{v2}, c_1, c_2, c_3 respectively.

And then, the variables of ghost fine cells at f_{v1} and f_{v2} can be calculated based on that at f'_{v1} and f'_{v2}, as follows:

$$U_{f_{v1}} = U_{f'_{v1}} + \frac{U_{f_1} - U_{f'_{v1}}}{x_{f_1} - x_{f'_{v1}}} (x_{f_{v1}} - x_{f'_{v1}}) \quad (3)$$

$$U_{f_{v2}} = U_{f'_{v2}} + \frac{U_{f_2} - U_{f'_{v2}}}{x_{f_2} - x_{f'_{v2}}} (x_{f_{v2}} - x_{f'_{v2}}) \quad (4)$$

where $U_{f_{v1}}, U_{f_{v2}}$ are the variables of ghost fine cells; U_{f1}, U_{f_2} are the variables at f_1 , f_2, respectively, which were calculated in the last time step; x_{f_1} , x_{f_2} , $x_{f_{v1}}$, $x_{f_{v2}}$, $x_{f'_{v1}}$ and $x_{f'_{v2}}$

are the coordinates in *x* directions at f_1 , f_2, f_{v1}, f_{v2}, $f_{v1}^{'}$, $f_{v2}^{'}$ respectively.

The values at f_{v1}, f_{v2} were used as the boundary conditions for the calculation of fine grids.

The variable interpolation from fine to coarse grids is presented in Figure 4(b), where one ghost coarse cell was established. The variables of ghost coarse cells were determined according to the fine and coarse grids between the interface. The variable interpolation may involve variables at locations $c_v^{'}, c_1, f_1, f_2$. As the variables are stored at the cell center, the variables at c_1, f_1, f_2 are available directly. The values at $c_v^{'}$ are obtained via natural neighbor interpolation, as follows:

$$U_{c_v^{'}} = U_{f_2} + \frac{U_{f_1} - U_{f_2}}{y_{f_1} - y_{f_2}}(y_{c_v^{'}} - y_{f_2}) \quad (5)$$

where $U_{c_v^{'}}, U_{f_1}, U_{f_2}$ are the variables at $c_v^{'}, f_1, f_2$ respectively; $y_{c_v^{'}}, y_{f_1}, y_{f_2}$ are the coordinates in *y* direction at $c_v^{'}, f_1, f_2$ respectively.

And then, the variables of ghost coarse cells at c_v can be calculated based on that at $c_v^{'}, c_1$, as follows:

$$U_{c_v} = U_{c_v^{'}} + \frac{U_{c_1} - U_{c_v^{'}}}{x_{c_1} - x_{c_v^{'}}}(x_{c_v} - x_{c_v^{'}}) \quad (6)$$

where U_{c_v} are the variables of ghost fine cells; U_{c_1} are the variables at c_1 ,which were calculated in the last time step; $x_{c_1}, x_{c_v^{'}}, x_{c_v}$ are the coordinates in *x* direction at $c_1, c_v^{'}, c_v$ respectively.

The values at c_v were used as boundary conditions for the calculation of coarse grids at the next time step.

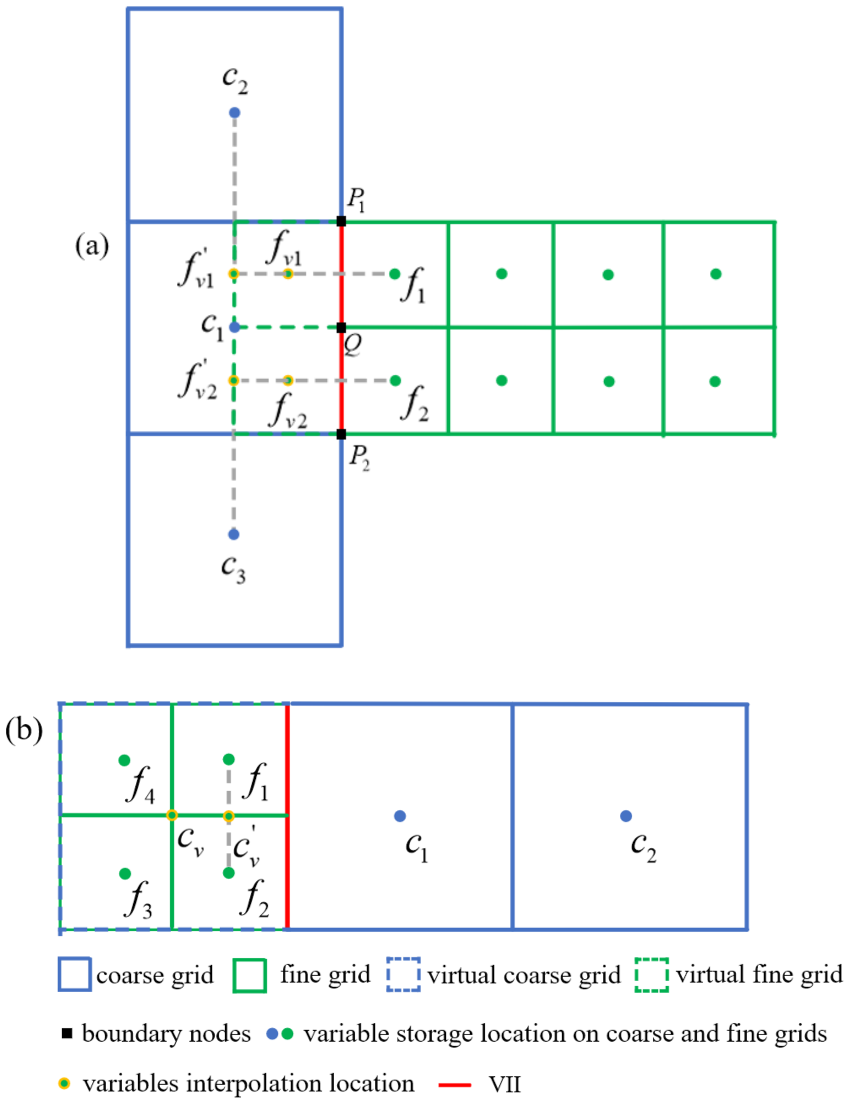

Figure 4. Variables interpolation between coarse and fine grids: (a) from coarse to fine grids and (b) from fine to coarse grids

2.3 Numerical models

2.3.1 Hydrologic model

In this study, referring to the runoff calculation in the Storm Water Management Model (SWMM), a 2D NLR model, including water balance and Manning equations, was used to simulate rainfall-runoff. In SWMM, the watershed is divided into many water tanks or reservoirs, where 1D NLR model including water balance and 1D Manning equations is used to simulate the runoff (Rossman, 2015). It is a simple and efficient method to calculate the runoff routing. In reality, however, the runoff routing is a 2D way, so it is not accurate to calculate the 2D runoff routing using 1D NLR model. Also, it is difficult to directly couple the 1D NLR model with 2D hydrodynamic model. Therefore, the 2D NLR model was used to simulate the 2D surface runoff routing in this study, as shown in Eqs. (7-11).

$$\frac{V_i^{n+1}-V_i^n}{\Delta t}=\left(Q_x\right)_{in\ i}-\left(Q_x\right)_{out\ i}+\left(Q_y\right)_{in\ i}-\left(Q_y\right)_{out\ i}+A_i q_{r\ i}^n \tag{7}$$

$$\left(Q_x\right)_{in\ i}-\left(Q_x\right)_{out\ i}=-\sum_{l=1}^{L}\left(q_{x\ \Gamma}^n\cdot n_x\right)_l \Delta L_l \tag{8}$$

$$\left(Q_y\right)_{in\ i}-\left(Q_y\right)_{out\ i}=-\sum_{l=1}^{L}\left(q_{y\ \Gamma}^n\cdot n_y\right)_l \Delta L_l \tag{9}$$

$$q_x=\frac{h^{5/3}S_x^{1/2}}{n_r} \tag{10}$$

$$q_y=\frac{h^{5/3}S_y^{1/2}}{n_r} \tag{11}$$

where the superscript n and n+1 is the time step; V is the water volume of grid (m^3); $\left(Q_x\right)_{in\ i},\left(Q_x\right)_{out\ i}$ is the inflow and outflow of grid i in x direction (m^3/s); $\left(Q_y\right)_{in\ i},\left(Q_y\right)_{out\ i}$ is the inflow and outflow of grid i in y direction (m^3/s); $q_{r\ i}$ indicates runoff rate of grid i (mm/h), which is rainfall intensity minus infiltration rate; A_i is the area of grid i (m^2); q_x, q_y are the unit discharge stored at cell-center along x and y direction (m^2/s), with h, u and v being water depth (m), flow velocity (m/s) in x and y directions, respectively; $q_{x\ \Gamma}, q_{y\ \Gamma}$ are the unit discharge at grid boundary in x and y direction, respectively (m^2/s), which are calculated based on q_x, q_y; ΔL_l is the side length of grid (m); l = 1, 2, 3, …, L is the number of edges of cell; n_r is the Manning roughness coefficient; S_x and S_y are water level gradients along x and y direction, respectively, $S_x = -\frac{\partial}{\partial x}\left(z_b + h\right), S_y = -\frac{\partial}{\partial y}\left(z_b + h\right)$, where z_b is the surface elevation.

2.3.2 Hydrodynamic model

The 2D SWEs, consisting of mass and momentum conservation equations (Toro 2001), were used to represent the hydrodynamic model.

$$\frac{\partial U}{\partial t} + \frac{\partial F}{\partial x} + \frac{\partial G}{\partial y} = S \tag{12}$$

$$U = \begin{pmatrix} h \\ hu \\ hv \end{pmatrix},\ F = \begin{pmatrix} hu \\ huu + gh^2/2 \\ huv \end{pmatrix}, G = \begin{pmatrix} hv \\ huv \\ hvv + gh^2/2 \end{pmatrix}, S = \begin{pmatrix} q_r \\ -gh\frac{\partial z}{\partial x} - \frac{g}{C^2}u\sqrt{u^2+v^2} \\ -gh\frac{\partial z}{\partial y} - \frac{g}{C^2}v\sqrt{u^2+v^2} \end{pmatrix}$$

where U is the conserved variables; F, G are the convection term in the x and y directions; S is the source term; C is Chezy's coefficient, $C = \frac{1}{n_r}R^{1/6}$,where n_r is the Manning roughness coefficient and R is the hydraulic radius.

The Finite Volume Method for Conservative Scheme was used to solve the SWEs, which can ensure local mass and momentum conservation in each control volume cell. The Eq. (12) can be discretized based on structured grids, as follows:

$$U_{i,j}^{n+1} = U_{i,j}^{n} - \frac{\Delta t}{A_{i,j}}\sum_{l=1}^{L}\left[F^l\left(U_{i,j}^n\right)dy - G^l(U_{i,j}^n)dx\right] + \frac{\Delta t}{A_{i,j}}S\left(U_{i,j}^n\right) \tag{13}$$

where the superscript n and n+1 is the time step; the subscript i, j refers to the grid i, j; dx and dy are the grid edge length. The meaning of other symbols is the same as before.

The Harten-Lax-van Leer contact (HLLC) approximate Riemann solver was used to solve the convection term. The second-order accuracy in temporal and spatial discretization was obtained based on the Runge-Kutta method and Monotone Upstream-centered Schemes for Conservation Laws (MUSCL) (Van Leer, 1979). The solution of SWEs was detailed in many references (Toro 2001).

2.4 Dynamic bidirectional coupling of hydrologic and hydrodynamic models

The hydrologic and hydrodynamic models were coupled dynamically and bi-directionally. A water depth threshold was defined in advance and used to determine the state of the cell. In a grid cell, if the water depth was lower than the predefined threshold, it was defined as a non-inundation region where the hydrologic model was applied. Conversely, if the water depth was higher than the threshold, it was considered an inundation region where the 2D hydrodynamic model was applied. When the rainfall intensity increased, the water depth increased because of the gradual accumulation of surface water volume. Once the water depth exceeds the predefined threshold, the non-inundation regions defined last time step may change to the inundation regions. The inflow discharge positions, flow path, and discharge values subsequently changed. Therefore, a CMI was formed between the inundation and non-inundation regions and the hydrologic and 2D hydrodynamic models were coupled bi-directionally through this CMI.

The hydrologic model is rational for the continuous non-inundation regions, and the hydrodynamic model is rational for the continuous inundation regions. However, since discontinuity existed at the CMI, the single hydrologic or hydrodynamic models were not acceptable, which was a challenge for the model calculation, as shown in Figure 5. The key issue with the coupled model was to establish a reasonable approach for determining the fluxes passing through the coupling interface, which should integrate the effect of the current flow state obtained from these two models on both sides of the coupling interface.

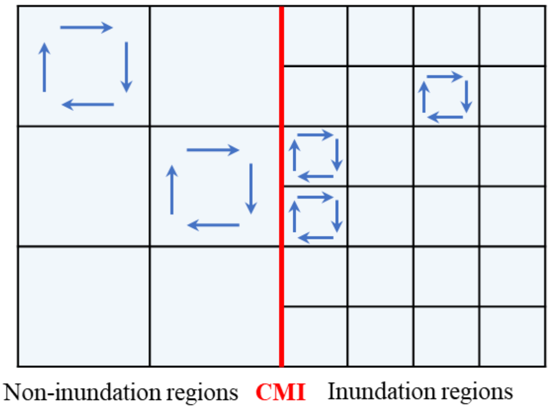

Figure 5 Model calculation at inundation regions, non-inundation regions and CMI

A pair of characteristic waves was used to determine the fluxes calculation methods through the CMI. The characteristic waves were calculated as follows:

$$S_L = u_{i,j} - \sqrt{gh_{i,j}} \tag{1}$$

$$S_R = u_{i+1,j} - \sqrt{gh_{i+1,j}} \tag{2}$$

where S_L and S_R are the characteristic waves; u is the flow velocity (m/s); h is the water depth (m); subscript (i, j) and (i+1, j) refer to the cells in non-inundation and inundation regions, respectively.

If $S_R > 0$ and $S_L > 0$, the fluxes through the CMI were calculated by the hydrologic model, and the CMI may move toward the non-inundation regions. Therefore, the non-inundation regions shrunk, whereas the inundation regions expanded. Only mass conservation through the CMI can be considered in this situation.

If $S_L < 0 < S_R$, the fluxes were calculated by both hydrologic and hydrodynamic models, and the CMI remained unchanged.

If $S_L < 0$ and $S_R < 0$, the fluxes are calculated by the hydrodynamic model, and the CMI may move toward inundation regions. Therefore, the inundation regions shrunk, whereas the non-inundation regions expanded. Both the mass and momentum conservation through the coupling boundary were obtained in the latter two situations.

The couplings were detailed in Jiang et al. (2021) and Shen et al. (2021).

2.5 Time step

An explicit scheme was used to solve the hydrologic and hydrodynamic models over time. The time step was constrained by the Courant-Friedrichs-Lewy condition (Delis and Nikolos, 2013), where the time step was a dynamic adjustment based on the velocity and water depth in the computational domain. Different time steps were adopted for the coarse and fine grids, and the time step of the fine grids was determined as follows:

$$\Delta t_f = C \cdot min\left(\frac{min\left(\Delta x_f\right)}{max\left(\left|u_f\right| + \sqrt{gh_f}\right)}, \frac{min\left(\Delta y_f\right)}{max\left(\left|v_f\right| + \sqrt{gh_f}\right)} \right) \tag{14}$$

where Δt_f is the time step of fine grids; C is a constant used to maintain format stability; Δx_f and Δy_f are the side lengths of fine grid in x and y directions; u_f and v_f are the flow velocities on fine grids along x and y directions, respectively; h_f is the water depth on fine grids.

The time step of the coarse grids (Δt_c) was determined based on that of the fine grids. If the size of the coarse grid was k times that of the fine grid, the time step of the coarse grid was determined to be $\Delta t_c = k\Delta t_f$.

3 Results

The performance of the IM-DBCM was analyzed by applying it to two 2D rainfall-runoff experiments and one real-world flooding process. And the OM-DBCM developed by Shen et al. (2021) was applied to the same cases for comparison with the IM-DBCM.

3.1 Rainfall over a plane with varying slope and roughness

In this case, a sloping plan measuring $500m \times 400m$ was designed, with slopes

$S_{ox} = 0.02 + 0.0000149x$ and $S_{oy} = 0.05 + 0.0000116y$ along the x and y directions, respectively (Jaber and Mohtar, 2003). The Manning coefficient is equal to $n = \sqrt{n_x^2 + n_y^2}$, where $n_x = 0.1 - 0.0000168x$ and $n_y = 0.1 - 0.0000168y$. The rainfall intensity is given by a symmetric triangular hyetograph $r = r(t)$,with $r(0) = r(200\,\text{min}) = 0$ and $r(100\,\text{min}) = 0.8 \times 10^{-5}\, m/s$. The total simulation time was 14,400 s.

Different cases with various grid resolutions were developed to divide the computational domain based on the D∞ algorithm, as listed in Table 1. In these cases, the size of all the fine grids was 1*m* × 1*m*. The grid discretization of different cases is shown in Figure S1 in Supplement.

Table 1 Different cases designed to simulate

Cases	The ratio of coarse to fine grids	Number of grids
case12	1:2	112,100
case15	1:5	86,840
case10	1:10	83,220

The hydrographs at the outlet node of coordinates of (500m, 400m) obtained from different models are shown in Figure 6. A model proposed by Jaber and Mohtar (2003) was also used to simulate the overland runoff. Because finer grids and small time step were used to divide the computational domain to obtain more accurate results in the model developed by Jaber and Mohtar (2003), the results calculated by Jaber and Mohtar (2003) can be used as a reference solution.

From Figure 6, the IM-DBCM held a shape close to the results simulated by Jaber and Mohtar (2003) in all cases, as well as the peak discharge. But the peak discharge of the hydrograph is slightly overestimated by the OM-DBCM, which may be attributed to the difference in the variable interpolation between the coarse and fine grids. In the

OM-DBCM, variables at the interpolation interface were equal to that at the cell center, which was then used to interpolate variables between the coarse and fine grids through shared and hanging nodes. This interpolation method had two drawbacks. Firstly, it is not reasonable to assume the variables at the interpolation interface are equal to that at the cell center, and the resulting error could increase as the grid size increases. Besides, compared with bilinear interpolation, the values at the hanging nodes are calculated by linear interpolation through shared nodes, which may result in relatively large errors. The results show that the methods to interpolate variable between the coarse and fine grids by developing ghost cells proposed in this study has acceptable accuracy.

To quantitatively assess the performance of IM-DBCM, the Root Mean Square Error (RMSE) of different cases was computed. The RMSEs of case12, case15 and case10 were 4.01E-04, 7.85E-03 and 3.25E-02, respectively. It is showed that the error gradually increased with the increasing of the ratio of coarse to fine grids. The IM-DBCM may capture the shape of the hydrograph in case12 and case15, both in limbs and peak discharge, but the peak discharge is slightly underestimated in case10. A possible explanation is that, compared to the coarse grids, the fine grids could better capture the geometry of the channel cross-sections. High-resolution grids can better represent small-scale topographic features and flow passages (Hou et al., 2018); consequently, the simulation results on case12 and case15 are more satisfactory than those on case10. Similarly, the simulation accuracy of the OM-DBCM also gradually decreased with the increasing of the ratio of coarse to fine grids. Overall, the benefit of using the IM-DBCM for the flood simulations is evident.

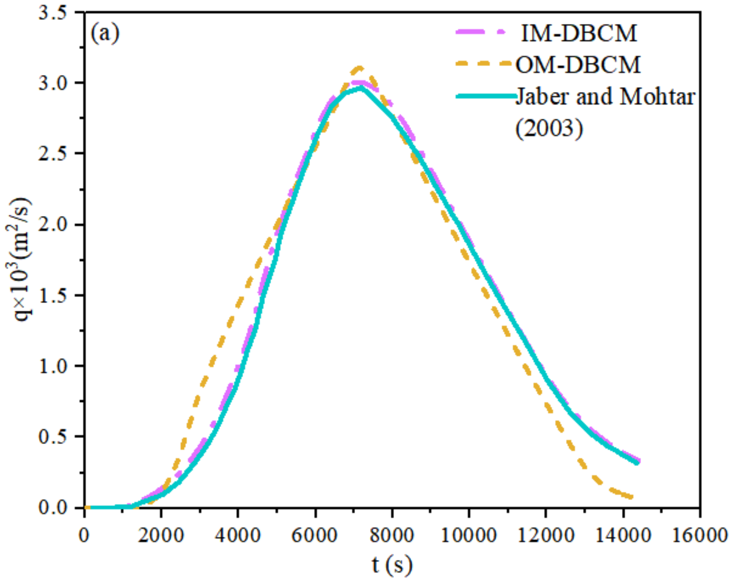
(a)
IM-DBCM
OM-DBCM
Jaber and Mohtar (2003)
q×10³(m²/s)
t (s)
0.0
0.5
1.0
1.5
2.0
2.5
3.0
3.5
0
2000
4000
6000
8000
10000
12000
14000
16000

416

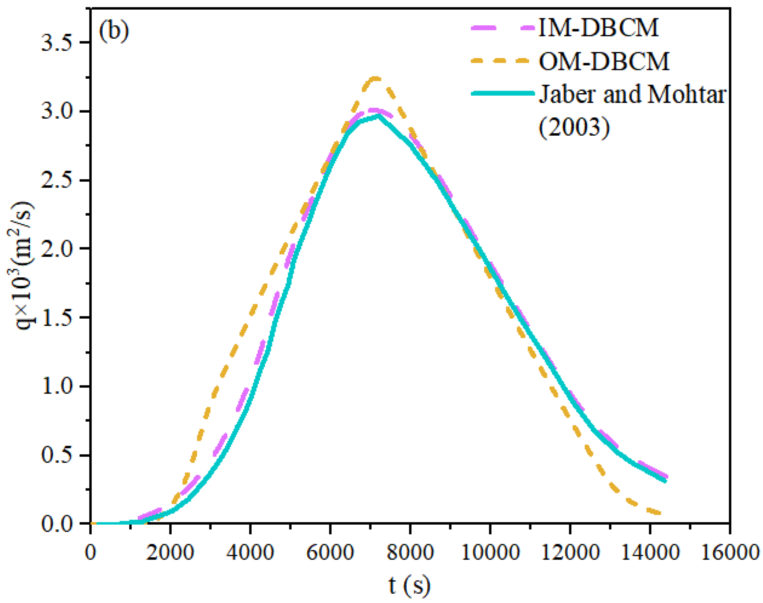
(b)
IM-DBCM
OM-DBCM
Jaber and Mohtar (2003)
q×10³(m²/s)
t (s)
0.0
0.5
1.0
1.5
2.0
2.5
3.0
3.5
0
2000
4000
6000
8000
10000
12000
14000
16000

417

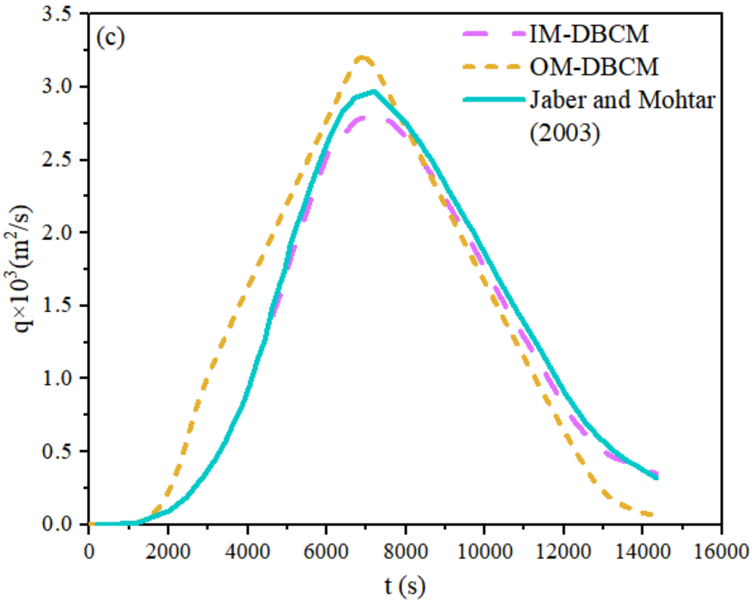

Figure 6 Hydrographs obtained from different models: (a) case12, (b) case15 and (c) case10

3.2 2D rainfall-runoff experiment

In this case, the IM-DBCM was used to compute the hydrograph generated by uniform rainfall conditions over a simple 2D geometry. The numerical results were compared with experimental data obtained in a laboratory model developed by Cea et al. (2008). The 2D geometry used in the experiment comprised a rectangular basin composed of three stainless-steel planes, each with a slope of 0.05. The basin had two walls that increased the residence time of the runoff in the basin and the length of the outlet hydrograph. The geometric dimensions of the basin are shown in Figure 7.

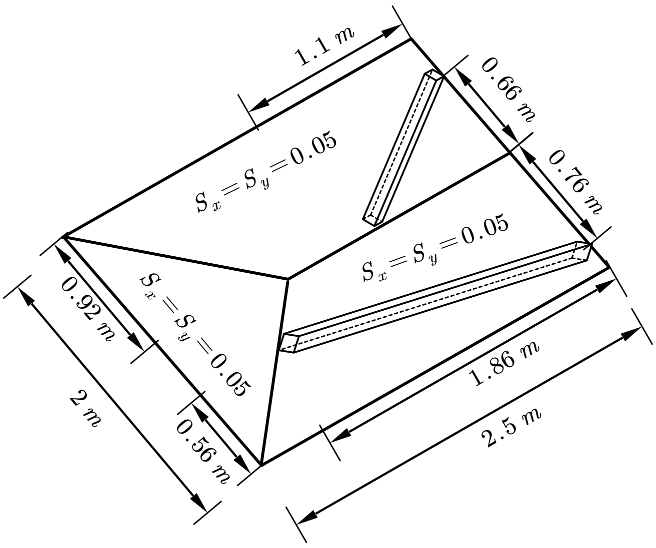

Figure 7. Geometry and size of the 2D basin for the rainfall-runoff experiment

Two rainfall intensities were simulated. In case01, the rainfall intensity was 317 mm/h for 45 s. In case02, the rainfall had an intensity of 320 mm/h for 25 s, then it stopped for 7 s and started again continuing for 25 s with an intensity of 328 mm/h.

The computational basin was divided into coarse and fine grids based on the D∞ algorithm. The size of the fine grids was 0.01m × 0.01m, whereas that of the coarse grids was 0.02m × 0.02m. The grid partition is presented in Figure S2 in Supplement. According to Cea et al. (2008), the Manning coefficient was 0.009 $s/m^{1/3}$.

Figure 8 shows a comparison between the numerical and experimental outlet hydrographs. The shape of hydrographs was well predicted in both cases, indicating that the IM-DBCM could capture the flow process and exhibited satisfactory accuracy. In case02, the first peak discharge rate occurred when the rainfall stopped for the first time. Subsequently, the discharge rate began to decrease. After 7 s, rainfall started again, and the discharge rate continued to decrease. The RMSEs of discharge simulated by IM-DBCM in case01 and case02 were 0.107 and 0.023, respectively. The numerical results were in good agreement with the experimental data. Compared to the results obtained from OM-DBCM, the simulation results obtained from IM-DBCM were closer to the experimental data. The results for case01 were slightly over-predicted by the OM-DBCM.

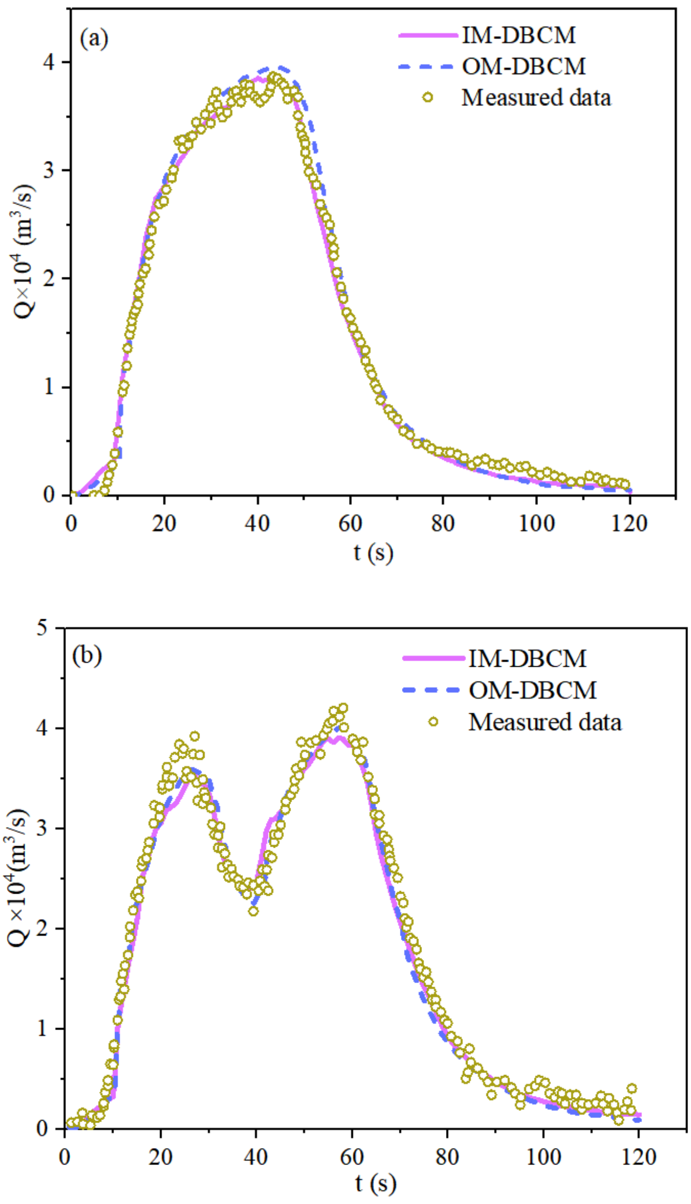

Figure 8. Simulated and measured discharge rate at different cases: (a) case01 and (b) case02

To verify the conservation of the IM-DBCM, the inflow and outflow of different cases were determined to represent the water balance, as shown in Figure 9. In case01, the outflow increased with the increasing of simulation time, whereas the water storage increased first and then decreased. When the rainfall stopped at 45 s, water was discharged from the basin; therefore, the water storage decreased. The sum of the outflow and storage was equal to the accumulated rainfall, indicating that the IM-DBCM can ensure the conservation of water mass. In case02, the outflow continuously increased. Two peak flows were observed for the water storage, which was caused by the intermittent rainfall. Overall, the sum of the outflow and water storage was equal to the accumulated rainfall, indicating that the IM-DBCM ensured mass conservation.

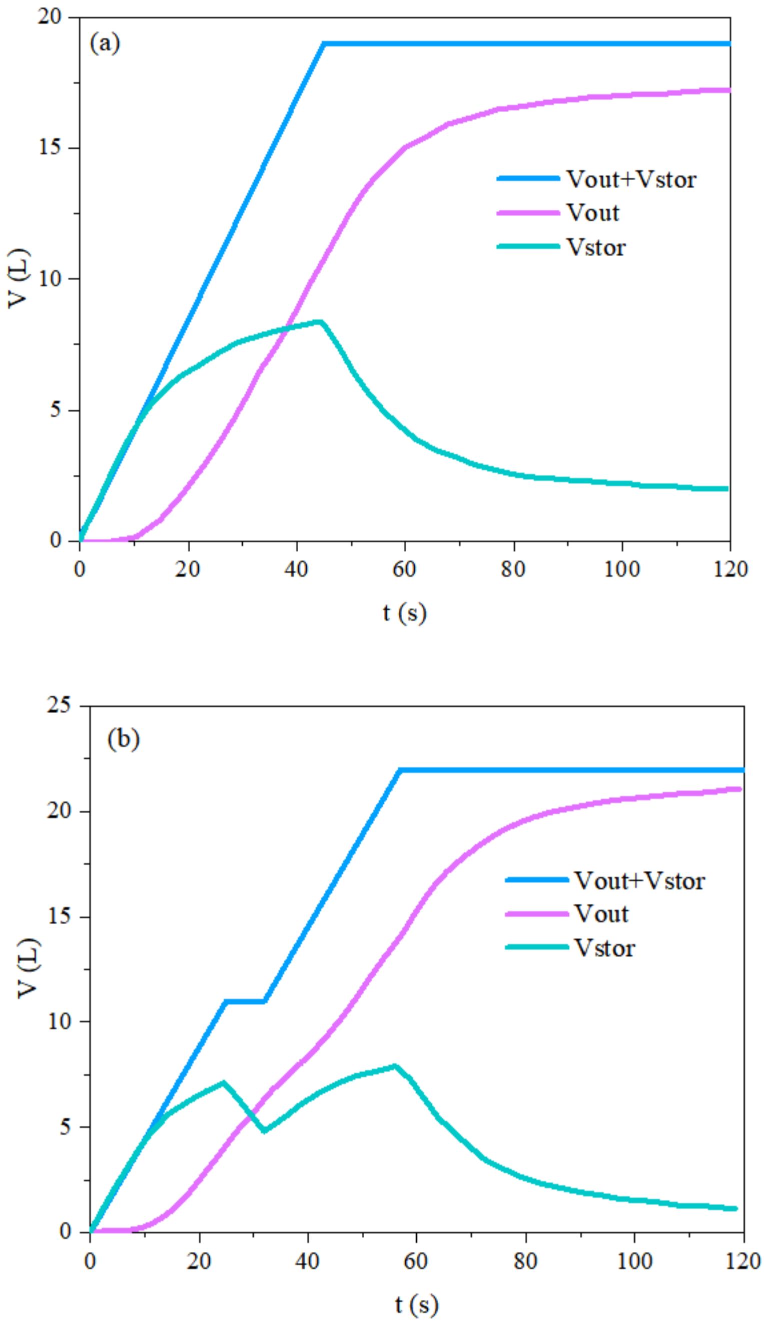

Figure 9. Inflow and outflow for different cases: (a) case01 and (b) case02, where

"Vout" refers to the outflow and "Vstor" refers to water storage in the computational basin

3.3 Flood simulation in a natural watershed

The Goodwin Creek watershed, located in Panola County, Mississippi, USA, is often selected as a benchmark to assess the capability of flood models because of sufficient available observed data. Drainage is westerly to Long Creek which flows into the Yocona River, one of the main rivers of the Yazoo River, a tributary of the Mississippi River. The Goodwin Creek watershed covers an area of 21.3 km^2. The overall terrain gradually decreased from northeast to southwest, which is consistent with the trend of the main channel, and the elevation ranged from 71 to 128 m. The computational basin and bed elevations are shown in Figure 10.

Land use in this watershed was divided into four classes including forest, water, cultivated, and pasture, and their Manning coefficients were 0.05, 0.01, 0.03, and 0.04, respectively (Sánchez, 2002). The infiltration coefficients of different soil types were determined according to Blackmarr (1995). The rainfall event in sixteen rain gages (see Figure 10) of October 17, 1981 was chosen for simulation (Sánchez, 2002), and the inverse distance interpolation method (Barbulescu, 2016) was used to calculate the precipitation over the entire watershed. The rainfall duration was 4.8 h. Rainfall was spatially distributed at different times, as shown in Figure S3 in Supplement. There were measured data in six observation stations (i.e., 1, 4, 6, 7, 8 and 14) (Blackmarr, 1995), whose locations were shown in Table S1 in Supplement, and the simulated results were compared with the measured data in these stations.

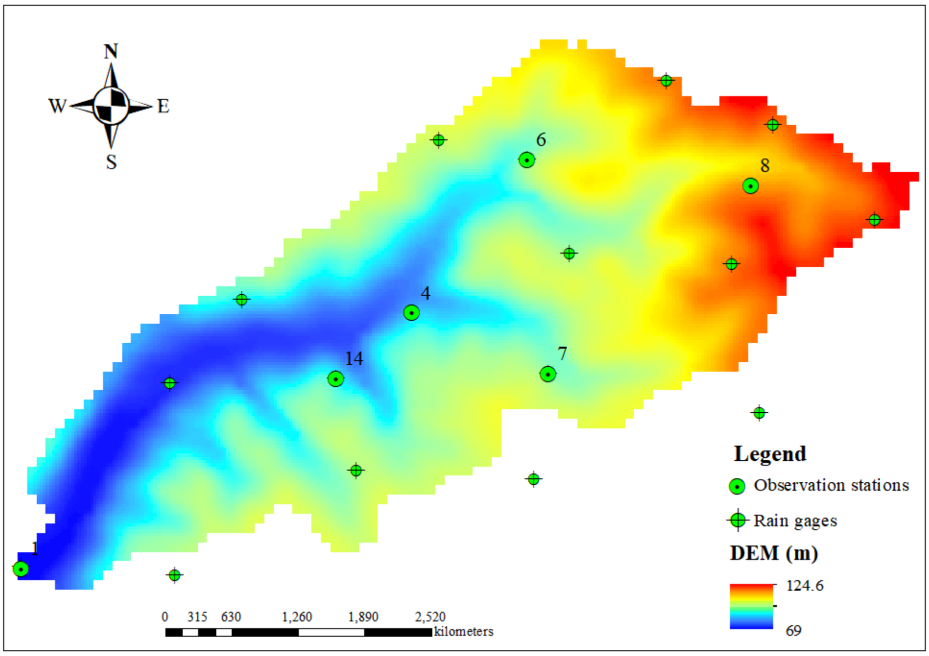

Figure 10. Overview of the Goodwin Creek watershed

The simulations were performed for 12 h. Different cases with various grid resolutions were developed to verify the computational efficiency and numerical accuracy of IM-DBCM, as listed in Table 2. In M-DBCM, the rivers were covered by fine-grid cells with dimensions of 10 m × 10 m, whereas the coarseness in the rest of the domain was increased to higher levels, as presented in Figure S4 in Supplement.

Table 2. Different cases designed to simulate the Goodwin Creek watershed

Cases	The ratio of coarse to fine grids	Number of grids
case12	1:2	104,555
case15	1:5	65,240
case10	1:10	59,431

The OM-DBCM was also used to simulate the rainfall runoff with the same resolutions. The Nash-Sutcliffe efficiency (NSE) was used to quantify errors in each model. The NSEs of IM-DBCM and OM-DBCM are shown in Table 3. From this table, the NSEs of IM-DBCM were higher than that of OM-DBCM at most stations, which was probably caused by the different interpolation method at the interface between coarse and fine grids. It is verified that the IM-DBCM has relatively high accuracy in simulating rainfall-runoff. In OM-DBCM, it is unreasonable to make the variables at the interface between coarse and fine grids equal to that at the cell center, which can bring errors. The induced error will increase as the ratio of coarse and fine grids increase. Therefore, it is also observed that the NSEs of OM-DBCM decreased with the increased ratio of coarse and fine grids. It is indicated that the ghost cells and bilinear interpolation used in the IM-DBCM to interpolate variables between coarse and fine grids can make the simulation more reasonable.

Table 3 NSEs of different models ("IM" and "OM" refer to IM-DBCM and OM-DBCM, respectively)

Station	G1		G4		G6		G7		G8		G14	
Model	IM	OM	IM	OM	IM	OM	IM	OM	IM	OM	IM	OM
case12	0.9496	0.9108	0.9611	0.9011	0.9904	0.8982	0.9658	0.9004	0.9435	0.9104	0.9311	0.8804
case15	0.9399	0.8766	0.9404	0.8800	0.9426	0.8819	0.9258	0.8931	0.9341	0.8942	0.9001	0.7942
case10	0.9207	0.8261	0.8907	0.8435	0.9513	0.7977	0.9358	0.8525	0.9358	0.8678	0.9135	0.8078

Figure 11 shows a comparison of the measured and simulated hydrographs by IM-DBCM at the monitoring gauges, whose locations are presented in Figure 10. At all gauges, the hydrographs obtained from different cases were well aligned with the measured data, which indicates that the IM-DBCM could reliably reproduce the flood wave propagation in the complex topography. The results of case12, in general, were better than those of case15 and case10, especially at station G1. A possible explanation is that a finer grid is needed to better capture the watershed geometry and obtain more satisfactory simulation accuracy. The cell size of case15 and case10 is larger than that of case12.

Compared with other stations, at station G1, the simulation results obtained from case15 and case10 deviated substantially from the measured data, especially at receding limb of the hydrographs. We deduced that the reason for this discrepancy is not the mesh partitioning, but the location of the G1. G1 is located at the watershed outlet, where water flows out of the watershed from here. The errors generated upstream may be accumulated at this station. Despite the deviation, the overall trend of the hydrographs indicated that the IM-DBCM is satisfactory and can reliably reproduce flood wave propagation in complex topography.

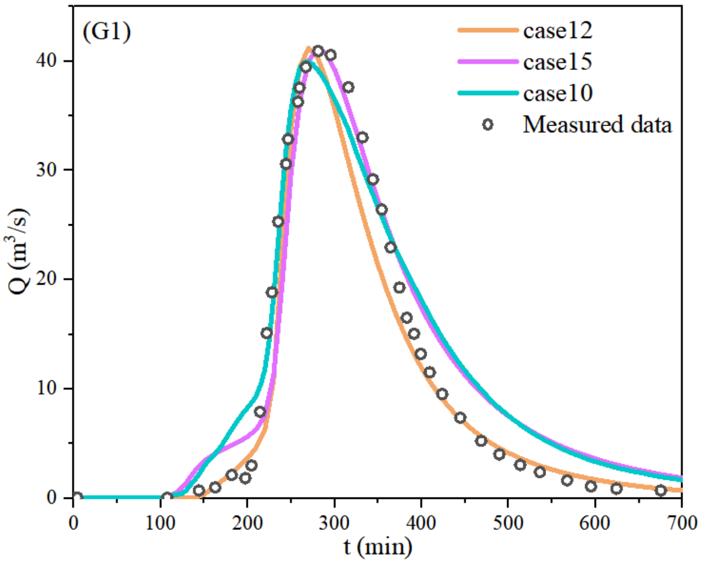

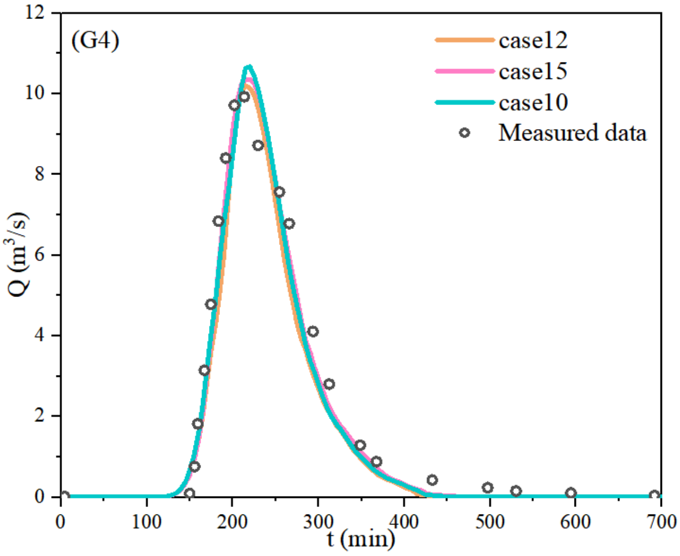

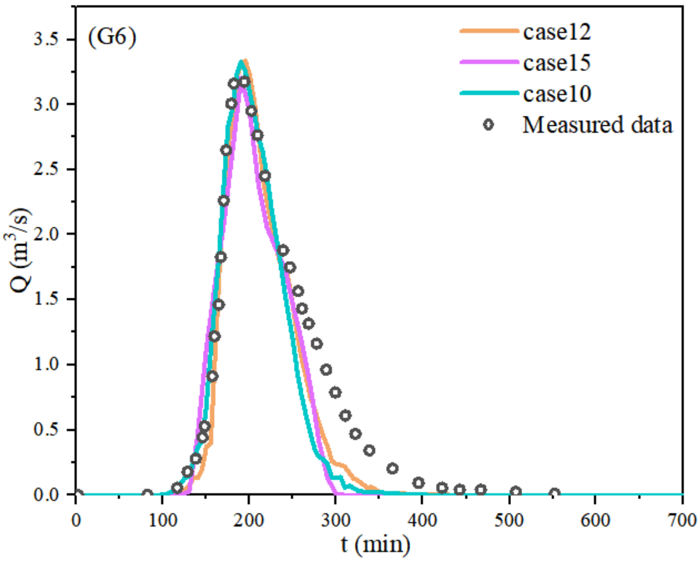
(G6)
case12
case15
case10
Measured data
Q (m^3/s)
t (min)

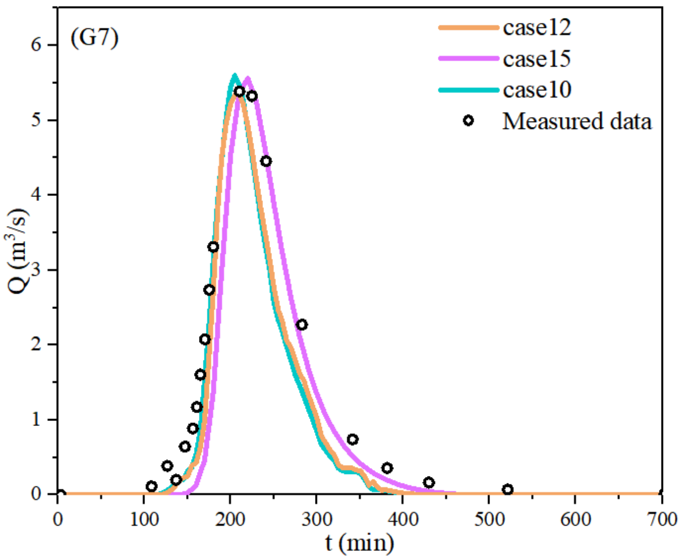
(G7)
case12
case15
case10
Measured data
Q (m^3/s)
t (min)

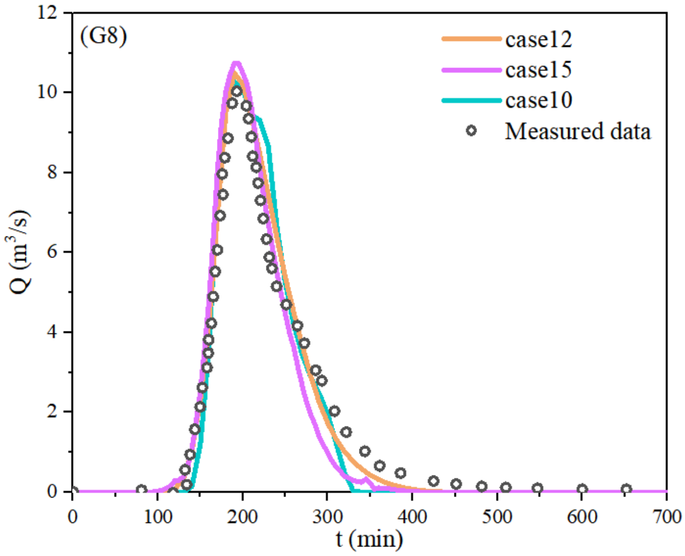
(G8)
case12
case15
case10
Measured data
Q (m^3/s)
t (min)

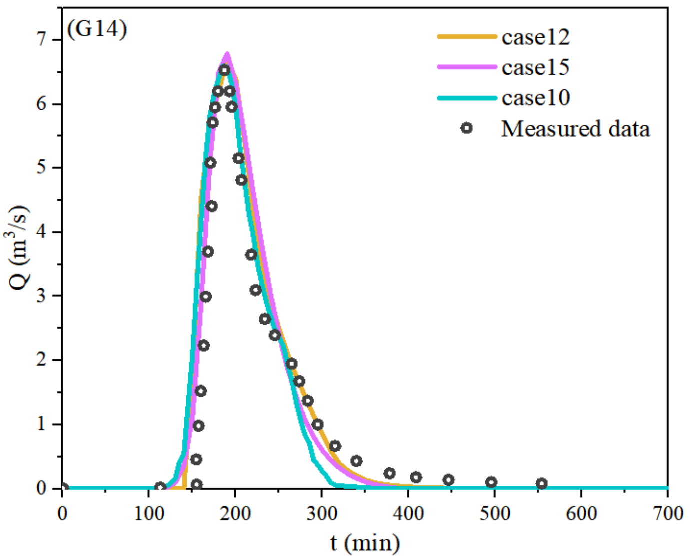

Figure 11. Hydrographs obtained from different cases

The water depth and location of the coupling interface at different times are shown in Figure 12. The position of the coupling interface was time-dependent. From 0 to 5 h, the water depth in the computational basin increased with the rainfall. Once the water depth was higher than the predefined threshold, the regions were defined as inundation regions and the hydrodynamic model was used to simulate the rainfall runoff. The water depth peaked in the watershed at 5 h, as shown in Figure 12(a1), and most of the regions were defined as inundation regions, as shown in Figure 12(a2). After 5 h, when rainfall stopped, the water depth in the computational basin decreased (Figure 12(b1)). When the water depth was lower than the predefined threshold, the inundation regions defined last time step became non-inundation regions. Accordingly, as shown in Figure 12(b2), the non-inundation regions expanded, whereas the inundation regions decreased. The location of the coupling interface was shifted to the inundation regions defined at the last time step. The results indicated that the coupling interface shifted during the simulation, which was consistent with the flood migration process.

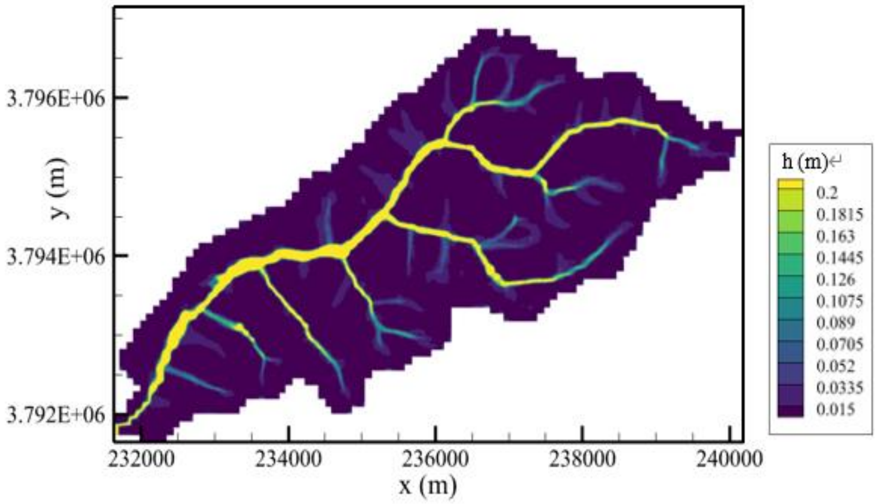

(a1) Water depth at t = 5 h

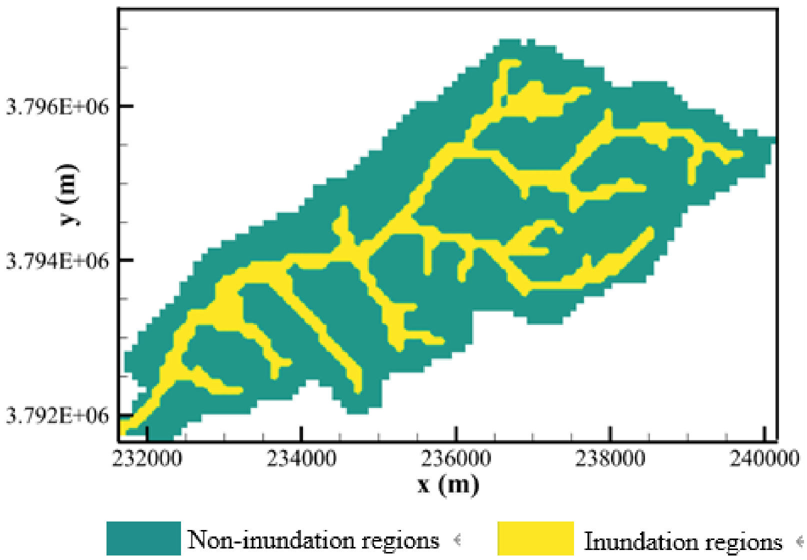

(a2) Position of the coupling interface at t = 5 h

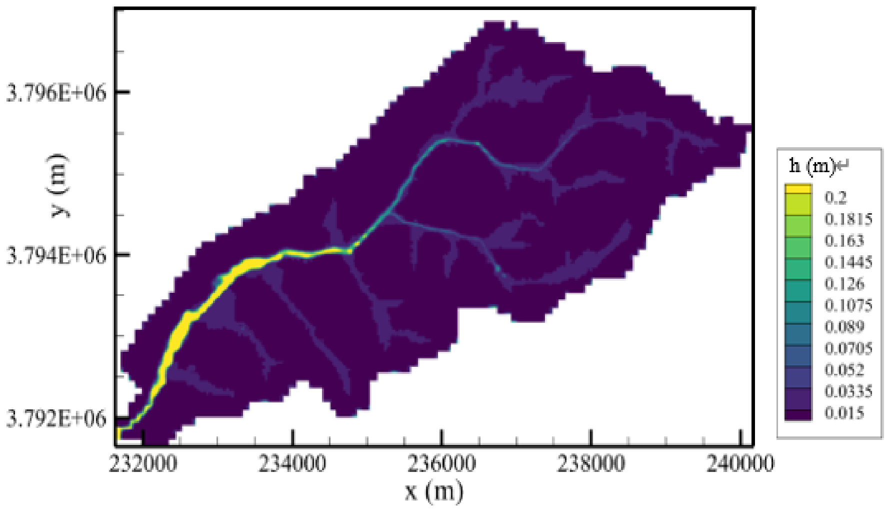

(b1) Water depth at t = 8 h

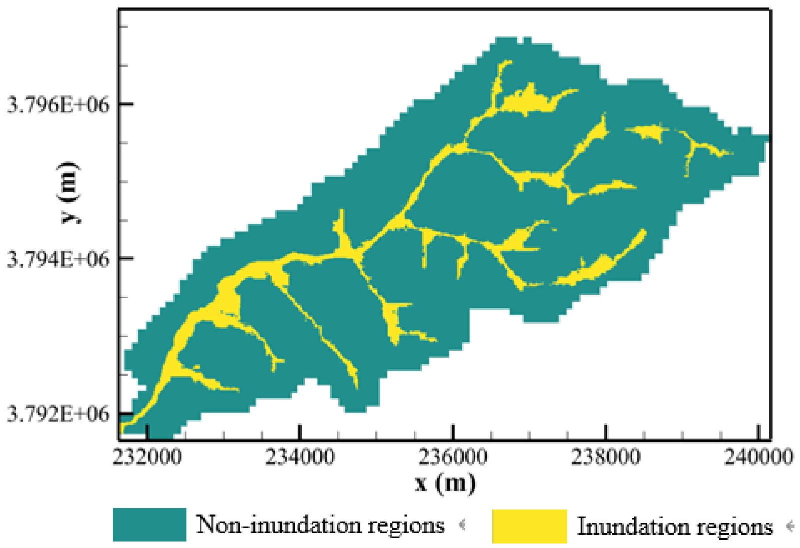

(b2) Position of the coupling interface t = 8 h

Figure 12. Water depth and position of the coupling interface of the hydrologic-hydrodynamic model at different times

In terms of efficiency, the total execution time of IM-DBCM was compared with the uniform grid-based model (case00), as shown in Figure 13. The total execution time of the different cases ranked from highest to lowest is as follows: case00> case12> case15> case10. Uniform fine grids were used to divide the computing zones in case00, and 207,198 computational grids were generated. Compared with case00, most of the areas were discretized with coarse grids, and only a small part of the regions was calculated based on fine grids in IM-DBCM; the computational grids of the multi-grid-based model (Table 2) were considerably lower than that of case00. The advantages of using IM-DBCM based on multi-grids for flood simulations are evident. The difference in total runtime between the IM-DBCM and OM-DBCM is the time spent on mesh generation. In the OM-DBCM, the computational domain is divided manually, which is highly subjective, and the computational time varied from person to person. Furthermore, case12 required more computational time than case15 and case10. Fewer computational grid nodes were presented in case15 and case10, which required less time for calculation, and the computational efficiency could be further improved.

However, there was not a significant difference in the computation time among these three cases. The calculation time for coarse grids is shown in Figure 13(b). It is observed that the runtime for coarse grids decreases rapidly in different cases. In case12, case15 and case10, the number of coarse grids is 42517, 7425, and 2153, respectively. As the number of coarse grids decreased significantly, the runtime for these grids also decreased rapidly. The number of fine grids is consistent in case12, case15, and case10, with a calculation time of 4800s. The fine grids number is much greater than that of the coarse grids, especially in case15 and case10. The 2D hydrodynamic model was solved in the fine-grid regions, which cost more computation time compared with the coarse grids where the hydrologic model was applied. The calculation time for fine grids is significantly longer than that for coarse grids, comprising a substantial portion of the overall execution time.

In many watersheds, the 2D inundation regions account for a minor proportion of the total watershed area. The fine grids were employed to partition the small inundation regions, while the coarse grids were utilized to discretize the majority of the non-inundation regions. The computational efficiency can be significantly enhanced due to the smaller proportion of fine grids and larger proportion of coarse grids. In the IM-DBCM, the 1D rivers and 2D inundation regions were not distinguished, resulting in their division using fine grids. Consequently, the 2D hydrodynamic model was applied to both regions, leading to an increased computational time. In future studies, the 1D hydrodynamic model will be used to compute the flood evolution specifically in the 1D rivers, leading to a reduction in computational time. Hence, the computational efficiency advantages of the proposed IM-DBCM are more pronounced.

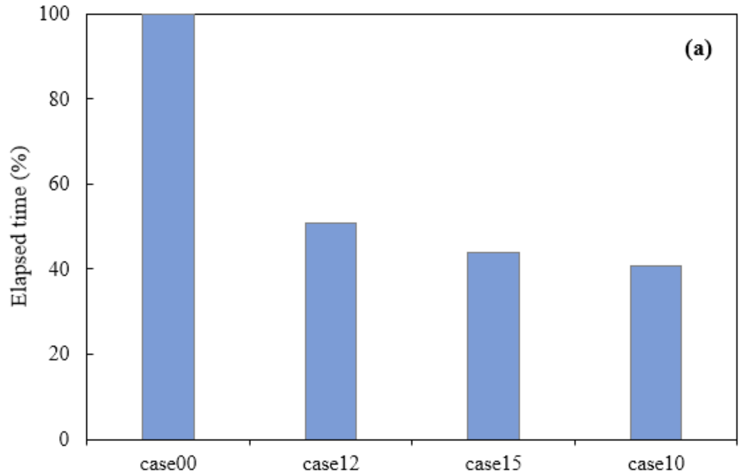

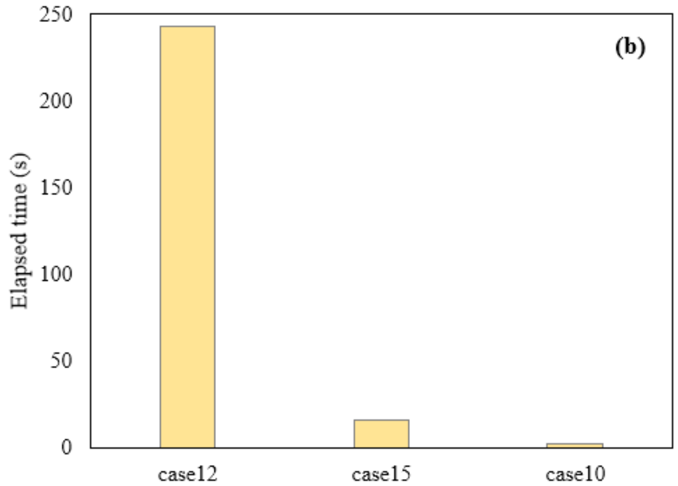

Figure 13 Computation time of different cases: (a) the relative difference of uniform-grid-based model and multi-grid-based models; (b) the runtime for coarse grids

4 Conclusions

An improved dynamic bidirectional coupled hydrologic-hydrodynamic model based on multi-grid (IM-DBCM) was presented in this study. A multi-grid system was generated based on the D∞ algorithm, dividing regions that required high-resolution representation using fine grids and the rest using coarse grids to reduce computational load. A two-dimensional non-linear reservoir was adopted in the hydrologic model, while two-dimensional shallow water equations were applied in the hydrodynamic model. The hydrologic model was applied to the coarse-grid regions, whereas the hydrologic and hydrodynamic models were coupled in a bidirectional manner for the fine-grid areas. Different time steps were adopted in coarse and fine grids. Ghost cells and bilinear interpolation were used to interpolate variables between coarse and fine grids. The hydrologic and hydrodynamic models were dynamically and bidirectionally coupled with a time-dependent and moving coupling interface.

The performance of IM-DBCM was verified using three cases. The IM-DBCM was demonstrated to effectively simulate flow processes and ensure reliable simulation. Compared with the OM-DBCM, the results obtained from the IM-DBCM were well aligned with the measured data, and it could reliably reproduce the flood wave propagation in complex topography. In addition to producing numerical results with similar accuracy, the IM-DBCM saved computational time compared with the model on fine grids. Furthermore, a moving coupling interface between the hydrologic and hydrodynamic models was observed in the IM-DBCM. The IM-DBCM has both high computational efficiency and numerical accuracy, which was adapted adequately to the real-life flooding process and provided practical and reliable solutions for rapid flood prediction and management, especially in large watersheds.

The IM-DBCM accurately and efficiently reproduces the flooding process and has the potential for a wide range of practical applications. Adding a one-way hydrodynamic model to the model could further enhance its performance. A one-way model can simulate flow in a narrow river, saving more time than using a two-way hydrodynamic model.

Data availability

Model simulation and calibration data are available upon request from the corresponding author. Digital elevation model data are provided by the Geospatial Data Cloud at http://www.gscloud.cn. The data sets of Soil Properties and Land cover are provided by Sánchez (2002) and Blackmarr (1995). The rainfall and measured data were Blackmarr (1995).

Author contributions

Yanxia Shen designed the methodology and carried out the investigation. Qi Zhou provided the original model input data. The study was supervised by Chunbo Jiang. Yanxia Shen prepared the first draft of the manuscript and Zhenduo Zhu revised and improved the original manuscript.

Competing interests

The authors declare that they have no conflict of interest.

Acknowledgements

This study was supported by the National Natural Science Foundation of China (Grant No. 52179068) and the Key Laboratory of Hydroscience and Engineering (Grant No. 2021-KY-04). The authors thank the anonymous reviewers for their valuable comments.

References

Barbulescu, A.: A new method for estimation the regional precipitation. Water Resources Management, 30(1), 33-42, 2016. https://doi.org/10.1007/s11269-015-1152-2

Bates, P.D.: Flood inundation prediction. Annual Review of Fluid Mechanics, 54：287-315, 2022. https://doi.org/10.1146/annurev-fluid-030121-113138

Bhola, P.K., Leandro, J., Disse, M.: Framework for offline flood inundation forecasts for two-dimensional hydrodynamic models. Geosciences (Switzerland), 8(9), 346, 2018. https://doi.org/10.3390/geosciences8090346

Blackmarr, W.: Documentation of hydrologic, geomorphic, and sediment transport measurements on the Goodwin Creek experimental watershed, northern Mississippi, for the period 1982-1993. Technical Report for United States

Department of Agriculture: Oxford, MS, USA, October, 1995.
Bomers, A., Schielen, R.M.J., Hulscher, S.J.M.H.: The influence of grid shape and grid size on hydraulic river modelling performance. Environmental Fluid Mechanics. 19(5), 1273-1294, 2019. https://doi.org/10.1007/s10652-019-09670-4
Cea, L, Puertas, J., Pena, L., Garrido, M.: Hydrologic forecasting of fast flood events in small catchments with a 2D-SWE model, Numerical model and experiment validation. World Water Congress, 1-4, Montpellier, France, 2008.
Caviedes-Voullième, D., García-Navarro, P., Murillo, J.: Influence of mesh structure on 2D full shallow water equations and SCS curve number simulation of rainfall/runoff events. Journal of Hydrology, 448-449(2), 39-59, 2012. https://doi.org/10.1016/j.jhydrol.2012.04.006
Choi, C.C., Mantilla, R.: Development and Analysis of GIS Tools for the Automatic Implementation of 1D Hydraulic Models Coupled with Distributed Hydrological Models. Journal of Hydrologic Engineering, 20, 06015005, 2015. https://doi.org/10.1061/(ASCE)HE.1943-5584.0001202
Costabile, P., Costanzo, C.: A 2D-SWEs framework for efficient catchment-scale simulations: hydrodynamic scaling properties of river networks and implications for non-uniform grids generation. Journal of Hydrology, 599(6402), 126306, 2021. https://doi.org/10.1016/j.jhydrol.2021.126306
Chen, W., Huang, G., Han, Z.: Urban stormwater inundation simulation based on SWMM and diffusive overland-flow model. Water Science and Technology 76(12):3392-3403, 2017. https://doi.org/10. 2166/wst.2017.504
Chen, W., Huang, G., Han, Z., Wang, W.: Urban inundation response to rainstorm patterns with a coupled hydrodynamic model: a case study in Haidian Island, China. Journal of Hydrology 564:1022–1035, 2018.

https://doi.org/10.1016/j.jhydrol.2018.07.069
Delis, A., Nikolos, I.: A novel multidimensional solution reconstruction and edge-based limiting procedure for unstructured cell-centered finite volumes with application to shallow water dynamics. International Journal for Numerical Methods in Fluids, 71: 584-633, 2013. https://doi.org/10.1002/fld.3674
Donat, R., Marti M.C., Martinez-Gavara, A., Mulet P.: Well-balanced adaptive mesh refinement for shallow water flows. Journal of Computational Physics, 257:937-53, 2014. https://doi.org/10.1016/j.jcp.2013.09.032
Ding, Z.L., Zhu, J.R., Chen, B.R., Bao, D.Y.: A Two-Way Nesting Unstructured Quadrilateral Grid, Finite-Differencing, Estuarine and Coastal Ocean Model with High-Order Interpolation Schemes. Journal of Marine Science and Engineering, 9(3), 335, 2021. https://doi.org/10.3390/jmse9030335
Feistl, T., Bebi, P., Dreier, L., Hanewinkel, M., Bartelt, P.: A coupling of hydrologic and hydraulic models appropriate for the fast floods of the Gardon river basin (France). Natural Hazards & Earth System Sciences, 14(11), 2899-2920, 2014. https://doi.org/10.5194/nhess-14-2899-2014
Garcia-Navarro P., Murillo J., Fernandez-Pato J., Echeverribar I., Morales-Hernandez M.: The shallow water equations and their application to realistic cases. Environmental fluid mechanics. 19(5): 1235-1252, 2019. https://doi.org/10.1007/s10652-018-09657-7
Ghazizadeh, M.A., Mohammadian, A., Kurganov, A.: An adaptive well-balanced positivity preserving central-upwind scheme on quadtree grids for shallow water equations. Computers & Fluids. 208, 104633, 2020, https://doi.org/10.1016/j.compfluid.2020.104633
Hu, R., Fang, F., Salinas, P., Pain, C.C.: Unstructured mesh adaptivity for urban

flooding modelling. Journal of Hydrology 560,354-363, 2018. https://doi.org/10.1016/j.jhydrol.2018.02.078

Hou, J., Wang, R., Liang, Q., Li, Z., Huang, M.S., Hinkelmann, R.: Efficient surface water flow simulation on static cartesian grid with local refinement according to key topographic features. Computers & Fluids, 176, 117-134, 2018. https://doi.org/10.1016/j.compfluid.2018.03.024

Hou J., Liu F., Tong Y., Guo K., Li D.: Numerical simulation for runoff regulation in rain garden using 2D hydrodynamic model. Ecological Engineering, 153(2), 105794, 2020. https://doi.org/10.1016/j.ecoleng.2020.105794

Jaber, F.H., Mohtar, R.H.: Stability and accuracy of two-dimensional kinematic wave overland flow modeling. Advances in Water Resources, 26(11): 1189-1198, 2003. https://doi.org/10.1016/S0309-1708(03)00102-7

Kim, J., Warnock, A., Ivanov, V.Y., Katopodes, N.D.: Coupled Modeling of Hydrologic and Hydrodynamic Processes Including Overland and Channel Flow. Advances in Water Resources, 37, 104-126, 2012. https://doi.org/10.1016/j.advwatres.2011.11.009

Kesserwani, G., Sharifian, M.K.: (Multi)wavelet-based Godunov-type simulators of flood inundation: Static versus dynamic adaptivity. Advances in water resources, 171,104357, 2023. https://doi.org/10.1016/j.advwatres.2022.104357

Jiang, C., Zhou, Q., Yu, W., Yang, C., Lin, B.: A dynamic bidirectional coupled surface flow model for flood inundation simulation. Natural Hazards and Earth System Sciences, 21(2), 497-515, 2021. https://doi.org/10.5194/nhes-21-497-2021

Moore, I.D., Grayson, R.B., Ladson, A.R.: Digital terrain modelling: a review of hydrological, geomorphological, and biological applications. Hydrological Processes, 5(1), 3-30, 1991. https://doi.org/10.1002/hyp.3360050103

Ozgen-Xian, I., Kesserwani, G., Caviedes-Voullieme, D., Molins, S., Xu, Z.X., Dwivedi, D., Moulton, J.D., Steefel, C.I.: Wavelet-based local mesh refinement for rainfall-runoff simulations. Journal of Hydroinformatics, 22(5), 1059-1077, 2020. https://doi.org/10.2166/hydro.2020.198

Rossman, L.A. Storm Water Management Model User's Manual Version 5.1; EPA/600/R-14/413b; U.S. Environmental Protection Agency: Cincinnati, OH, USA, 2015.

Schumann, G.J.P., Neal, J.C., Voisin, N., Andreadis, K.M., Pappenberger, F., Phanthuwongpakdee, N., Hall, A.C., Bates, P.D.: A first large-scale flood inundation forecasting model. Water Resource Research 49(10):6248–6257, 2013. https://doi.org/10.1002/wrcr.20521

Sánchez, R.R.: GIS-Based Upland Erosion Modeling, Geovisualization and Grid Size Effects on Erosion Simulations with CASC2D-SED. Ph.D. Thesis, Colorado State University, Fort Collins, CO, USA, 2002.

Singh J., Altinakar M.S., Yan D.: Two-dimensional numerical modeling of dam-break flows over natural terrain using a central explicit scheme. Advances in Water Resources, 34(10), 1366-1375, 2011. https://doi.org/10.1016/j.advwatres.2011.07.007

Seyoum. S.D., Vojinovic, Z., Price, R.K., Weesakul, S.: Coupled 1D and noninertia 2D flood inundation model for simulation of urban flooding. Journal of Hydraulic Engineering 138(1):23–34, 2012. https://doi.org/10.1061/(ASCE)HY.1943-7900.0000485

Shen, Y., Jiang, C., Zhou, Q., Zhu, D., Zhang, D.: A Multigrid Dynamic Bidirectional Coupled Surface Flow Routing Model for Flood Simulation. Water, 13, 3454, 2021. https://doi.org/10.3390/w13233454

Shen, Y., Jiang, C.: Quantitative assessment of computational efficiency of numerical models for surface flow simulation. Journal of Hydroinformatics, 25 (3): 782–796, 2023. https://doi.org/10.2166/hydro.2023.131

Tarboton, D.G.: A new method for the determination of flow directions and upslope areas in grid digital elevation models. Water Resources Research, 33(2), 662-670, 1997. https://doi.org/10.1029/96WR03137

Toro, E.F.: Shock-Capturing Methods for Free-Surface Shallow Flows. John Wiley, 2001.

Thompson, J.R., SoRenson, H.R., Gavin, H., Refsgaard, A.: Application of the coupled MIKE SHE/MIKE 11 modelling system to a lowland wet grassland in southeast England. Journal of Hydrology, 293(1-4): 151-179. 2004. http://doi.org/10.1016/j.jhydrol.2004.01.017

US Army Corps of Engineers, HEC-RAS User's Manual (version 6.4), 2023.

Van Leer, B.: Towards the ultimate conservative difference scheme V: A second order sequel to Godunov's method. Journal of Computational Physics, 32(1), 101-136, 1979. https://doi.org/10.1016/0021-9991(79)90145-1

Wing, O., Sampson, C.C., Bates, P.D., Quinn, N., Neal, J.C.: A flood inundation forecast of hurricane Harvey using a continental-scale 2D hydrodynamic model. Journal of Hydrology X, 4, 100039, 2019. https://doi.org/10.1016/j.hydroa.2019.100039

Yu, W.: Research on Coupling Model of Hydrological and Hydraulics Based on Adaptive Grid. Ph.D. Thesis, Tsinghua University, Beijing, China, 2019.

Xia, X., Liang, Q, Ming, X.: A full-scale fluvial flood modelling framework based on a high-performance integrated hydrodynamic modelling system (HiPIMS). Advances in Water Resources, 132, 103392, 2019.

https://doi.org/10.1016/j.advwatres.2019.103392